Global thermal image of cylindrical 21700 Li-ion batteries with distributed optical fibre sensor

Zhen Guo [*], Calum Briggs, Timothy A. Vincent, Begum Gulsoy, Jonathan E.H. Sansom, James Marco

Warwick Manufacturing Group (WMG), University of Warwick, Coventry, CV4 7AL, United Kingdom

HIGHLIGHTS

- Cylindrical cells with optical fibre sensors for the global thermal image.
- Distributed optical fibre sensors presented with mm-level spatial resolution.
- Thermal gradient observation along the circumference of the cell.
- Correlation between cell tabs' location and heat generation.

ARTICLE INFO

ABSTRACT

The ability to monitor the thermal behaviour of lithium-ion batteries (LIB) is an essential pre-requisite to optimise performance and ensure safe operation. However, traditional point measurement (thermocouples) faces challenges in accurately characterising LIB behaviour and notably in defining the hotspot and the magnitude and direction of the thermal gradient. To address these issues, an optical-frequency-domain-reflectometer (OFDR) based distributed-optical-fibre-sensor has been employed to quantify the heat generation within a cylindrical 21700 LIB. A 3 mm spatial resolution within the optical sensor is realised. The optical fibre has been wound around the cell surface for over 1300 unique measurement locations; distributed around the circumference and axially along the LIB. Distributed measurements show the maximum thermal difference can reach 8.37 °C during a 1.5C discharge, while the point-like sensors have 4.31 °C thermal difference. While a temperature gradient along the cell axial length is well understood, for the first time, this research quantifies the temperature variations along the circumference of the cell. The global thermal image highlights heat generation is accumulated around the positive current tab, implying that a fundamental knowledge of internal LIB structure is required when defining sensor placement within the traditional characterisation experiments and deployment within the battery management system (BMS).

1. Introduction

During the ongoing transition from fossils fuels to renewable energy, Li-ion batteries play an essential role as one of the most versatile energy storage technologies. Their increasing energy density and gravimetric helps to advance the rechargeable Li-ion batteries to ranges of strategic industries such as automotive, power grid, aerospace and consumer electronics. However, such broader application has always been challenged by factors such as cost, lifespan, durability, and susceptibility to unexpected failure. High chemical energy can be abruptly released in the form of fires or explosions if operated improperly. For example, the Tesla electrical car battery fire [1], the Boeing 787 battery problems [2] and Samsung Note mobile explosions [3], have attracted massive media concern. These incidents continuously remind the safety must remain the predominant factor for batteries.

Two methods are usually explored to ensure the battery safety: internal or external protection. Internal protection relies on the intrinsically safe materials [4–6], cell components [7,8] and cell format [9,10]. On the other hand, external protection focuses on the accurate monitoring the functional statue for batteries management, such as current, voltage, temperature, pressure and strain. Temperature is critical to the

---

Nomenclature

Abbreviation

BMS	Battery Management System
BOTDR	Brillouin Optical Time Domain Reflectometer
BTMS	Battery Thermal Management System
CC	Constant Current
CT	Computerised tomography
CV	Constant Voltage
DAQ	Data Acquisition Card
EFR	Equal Frequency Resample
FBG	Fibre Bragg Grating
FUT	Fibre Under Test
LIB	Lithium Ion Battery
LiNiMnCoO$_2$	Lithium Nickel Manganese Cobalt Oxide
LO	Local Oscillator
OFDR	Optical Frequency Domain Reflectometer
OFS	Optical Fibre Sensor
OPD	Optical Path Delay
OTDR	Optical Time Domain Reflectometer
PD	Photon Detector
TC	Thermocouples
TLS	Tuneable Laser Source

Symbol description Unit

z	Position, m	
I	Light intensity, W	
E	Electrical field of light, V	
c	Speed of light, m/s	
n	Refractive index	
T	Temperature, $^{\circ}$C	
β	Wave number, m^{-1}	
ε	Permittivity, F/m	
γ	Wavelength sweep speed, nm/s	
τ_z	Time delay of position z, s	
φ	Phase, $^{\circ}$	
K_T	Optical fibre thermal coefficient, $^{\circ}$C^{-1}	

---

performance, durability and safety of Li-ion batteries. Low temperature or overheat will greatly deteriorate the batteries performance. The best operating temperature are defined between 25 °C and 40 °C [11,12]. Excessively heat can lead to breakdown of solid electrolyte interface, decomposition of electrolyte and even explosive thermal runaway.

With the current trend of larger format and increasing cell number in one pack for high energy density, following challenges are proposed for the temperature monitoring in the current battery thermal manager system (BTMS) 1). Larger cells and/or module will experience more significant and complex thermal gradient during operation. With the cell size expanding from 18650, 21700 to 46800, from the cylindrical cells to pouch/prismatic cells, point-like sensor cannot provide accurate and reliable heat characterisation and sometimes will miss the hotspot generation for the hazard alarm. The radial temperature distribution inside a cylindrical 18650 cells is studied to optimise the cooling conditions, and further validate electrochemical-thermal coupled battery models [13]. It is found that thermal gradients perpendicular to the stack of pouch cells can lead to higher local currents and faster degradation compared to in-plane thermal gradient [14]. 2). Theoretically, BTMS requires accurate sensing of each cell for the model parameterisation and management. But commercial battery pack usually has limited sensors due to the issue of volume/cost/complexity. Take Tesla Model 3 for example, one battery pack has nearly 7104 cells. But current EV systems typically have limited sensors less than 20. 3). Besides the cell surface, the internal sensing can provide a more accurate understanding and state prediction. By instrumenting an optical sensor inside the cylindrical 21700 cells, the maximum temperature difference between the cell core and surface can be high to 9.7 °C [15]. Smart cell with an array of thermistors is constructed for the internal core temperature sensing, which observe 2.8 °C thermal gradient along the axial direction of a cylindrical [16]. Such cell internal monitoring usually requires the sensors with extra mechanical robustness, immunity to electromagnetic radiation, resistance to corrosion and low invasiveness.

Optical fibre sensor is a promising methodology to address the discussed issues. Compact size of sub-millimetre diameter and composition of silica enables the convenient instrumentation and minimum influence on cell performance. Infrared camera is also used to record the thermal picture of operations cells [17,18]. It has competitive sensing resolution and accuracy. But the cell's pre-painting to black, limited vision of the camera aperture and oversized setup makes it difficult to integrated to current battery thermal management system. Varieties of optical fibre sensors based on fibre Bragg grating, optical interferometer, evanescent waves and photo-luminescent, have been investigated for batteries [19].

The FBG sensor was first integrated in Li-ion batteries to measure temperature variations in 2013 [20]. Nascimento et al. presented an in-situ and in-operando temperature monitoring approach of Li-ion batteries. The internal and external temperature variations were measured by integrating two internal FBG sensors and two external FBG sensors in Li-ion pouch cells [21]. Customized optical fibre birefringent sensors based on FBG-PANDA have been developed and employed to instrument a cylindrical 18650 cell to track temperature and radial strain simultaneously [22]. Compared to the point-like and semi-distributed FBG array sensors, scattering-based optical fibre sensor can provide the real distributed measurement, allowing all-fibre sensing [23,24]. Optical frequency domain reflectometer (OFDR) [25] with a tuneable laser source is able to deliver distributed measurement as well as a fine resolution, which makes it a preferable candidate for the battery thermal monitoring.

In our previous study, a distributed optical fibre sensor with ultimate sub-mm spatial resolution is realised by efficient suppression of laser nonlinear sweep and phase noise [26,27]. Therefore, in this paper, we utilise this OFDR-based distributed sensor to investigate the surface thermal of cylindrical 21700 cells. In the first section, principle of distributed optical sensor and cell instrumentation with optical fibre sensor is discussed. Under the merit of compact size and fine resolution, the optical fibre sensor is instrumented on the 21700 cells for the global surface thermal image. Further relationship between thermal generation and cell current tab is discovered and investigated. In the last section, both point-like thermocouple and optical fibre sensor are studied to further validate the cell thermal behaviour.

2. Experimental method

2.1. Distributed optical fibre sensor

It is beyond the scope of this paper to discuss, in detail, the underpinning principles of employing a distributed optical fibre sensing method. However, a summary is provided below for completeness [26].

2.1.1. Principle of operation

Optical frequency domain reflectometer is one of the Rayleigh backscattering-based distributed optical fibre sensing methods. The basic configuration of an OFDR comprises a tuneable laser source and an optical interferometer, as shown in Fig. 1 (a). The fibre under test (FUT) lies in one arm of the interferometer. A non-idealistic optical fibre refractive index will inevitability lead to random Rayleigh
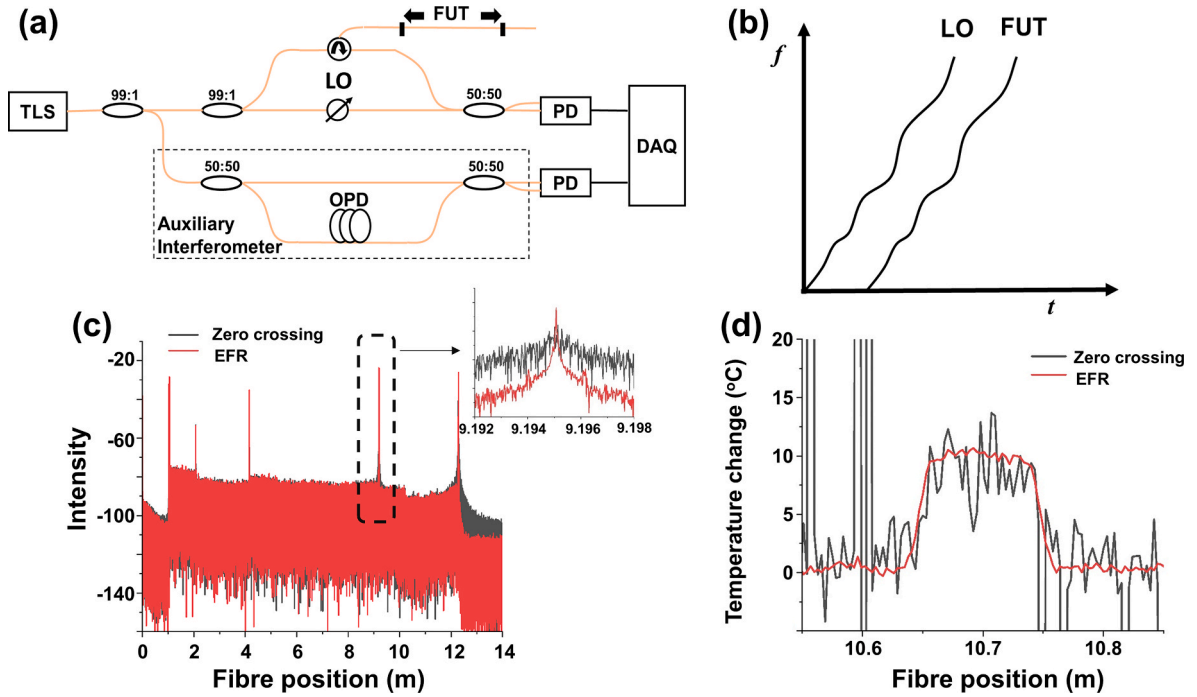
Fig. 1. (a) Schematic diagram of optical frequency domain reflectometer [26]. (b) Nonlinear sweep noise of the tuneable laser source [26]. (c) Spectrum distribution of fibre under test. Inset - Comparison of spatial resolution between the zero crossing resample and equal frequency resample (EFR). (d) Distributed temperature measurement with 3 mm resolution.

backscattering along the length of the FUT. Therefore, while a tuneable laser source with wavelength sweep speed γ launches into the FUT, the interference between the Rayleigh backscattering at position z on the FUT and the reference arm of the local oscillator (LO) can be expressed as:

$$I(t) = E(z)^2 \, cos\left[2\pi\left(v_0\tau_z + \gamma\tau_z t - \frac{1}{2}\gamma\tau_z^2\right) + \varphi_n(t,\tau_z)\right] \qquad (1)$$

where τ_z is the time delay between the position z in the FUT and the reference arm LO. v_0 and φ_n denote the initial frequency and phase noise respectively. The position of z along the fibre corresponds to the beat frequency of $\gamma\tau_z$. The term beat frequency defines the specific Rayleigh backscattering happening at position x. The linear wavelength sweep provides the position information along with the FUT.

To realise each unique temperature measurement, the variation of the randomly distributed permittivity in the fibre is introduced by filtering the specific spatial frequency components [28]:

$$\int_{-\Delta\beta}^{\Delta\beta} I_d(\beta - \beta_0)\exp(-i\beta x)d\beta = E_0^2 r \frac{c\pi\beta_0}{ni}\Delta\bar{\varepsilon}^*\left(z_0 + \frac{x}{2}\right) \qquad (2)$$

where β_0 is the detected wave number, $\Delta\beta$ is the range of measurement wave number, r is the reflectivity of the Rayleigh scattering, $\Delta\varepsilon$ is the variation of permittivity at the certain spatial frequency components, c is light speed, z_0 is the center position on the corresponding sensor, x is the sensing resolution. A cross correlation of the spectrums between the section with and without temperature variation is conducted for the frequency shift Δv, which is related to the corresponding applied temperature:

$$\frac{\Delta v}{v} = -K_T \Delta T \qquad (3)$$

where v is the mean optical frequency and K_T is the optical fibre thermal coefficient. It is noteworthy that the optical fibre sensor measures the temperature variation, not the absolute temperature value. Therefore, additional calibration is required before experimental measurement.

2.1.2. Nonlinear sweep noise

With the wavelength sweep range (in the order of 10–100 nm), OFDR has the theoretical capability to retain a fine distributed measurement with a spatial resolution of less than 1 mm. However, there are intrinsic noise that must be addressed to obtain a reliable and robust measurement. Fig. 1(b) represents the nonlinear sweep of the laser source. Such nonlinear noise would cause random frequency deviation during the LO and FUT interference, which further blurs the position identification adding uncertainty to the measurement.

The use of auxiliary interferometer shown in Fig. 1(a) is an efficient method to estimate and compensate for such nonlinear noise. In our previous works [26,27], equal frequency resample (EFR) and random wavelength-range calibration are proposed as viable methods to suppress this noise and deliver accurate sub-mm spatial resolution measurements. Fig. 1(c) shows the comparison between our proposed EFR technique and the use of conventional zero crossing resampled measurement methods. In this study, the length of the FUT is 12 m. The optical fibre sensor is Corning SMF-28e+. Measured intensity peaks at circa: 1 m, 4 m, 9 m and 12 m are optical connectors. With a sweep wavelength range of 30 nm, the measured peak width at the location 9.19 m is found to be 30.12 μm (inset in Fig. 1(c)). This is close to the theoretical limit of 27.4 μm ($\Delta z = c/2n\nu_{scan}$), proving the efficient elimination of nonlinear sweep noise. Conversely, as shown in inset of Fig. 1(c), the conventional zero-crossing resampling method cannot identify the peak at the same level of spatial resolution (e.g. 3 mm). To realise the distributed measurement with a 3 mm spatial resolution, each 109 points in Fig. 1(c) are filtered by a slide-window for calculating the frequency shift Δv, which is related to the temperature variation defined in (Eq. (3)).

The distributed optical temperature measurement is shown in Fig. 1 (d). The chamber temperature changes from 25 °C to 35 °C. Conventional zero crossing cannot perform stable measurement due to various noise, while the proposed EFR can provide a fine distributed measurement. Such temperature measurement with small deviation and a fine resolution proves the proposed OFDR for the thermal monitor in compact cylinder cells.

2.2. Cell specification and instrumentation

2.2.1. LIB specification

The candidate LIB employed in this research is a LG INR21700 M50 with a 4.85Ah nominal energy capacity. The cathode comprises a $LiNiMnCoO_2$ material paired with a graphite anode. The cell operates between a lower and upper voltage of 2.50V–4.20V respectively. The maximum charge and discharge rates are 0.7C and 1.5C respectively. A cylindrical rechargeable 21700 LIB is utilised here because: (1) this represents one of the most common formats, highlighting the practical value of the *global thermal image* for reliable cell characterisation and system design, (2) the physical size is sufficiently small to easily demonstrate the use and value of the OFDR technique for quantifying temperature gradients and location variability for the cell's hotspot and finally, (3) the cylindrical structure inherently provides a more challenging surface to instrument compared to larger prismatic or pouch cell formats.

Computerised tomography (CT) scanning of the cylindrical cell is shown in Fig. 2. TESCAN UniTOM XL is used for the non-destructive imaging and VGStudio employed for post-image analysis. The dimensions of the cell comprise a diameter of 21.20 mm and height of 70.10 mm. The cross-section of the cell is shown in Fig. 2 (a). The architecture of the cell includes one positive current tab and one negative current tab. The positive current tab is located within the jellyroll (between the 8th and 9th layers), while the negative current tab is placed between the jellyroll and the internal of the battery wall. The corresponding angle between two tabs is measured at 95.88 °C. The longitudinal sections of both tabs are shown in Fig. 2 (b, c). The positive current tab starts from the positive cap with a length of 61.98 mm. Conversely, the negative current tab starts from the bottom with a length of 33.90 mm towards the centre of the cell. The unrolled image of both the positive and negative current tabs is presented in Fig. 2 (b)-right and (c)-right. The widths of the positive and negative tabs are measured at 4.14 mm and 3.85 mm respectively. Section 3 highlights the correlation between tab position, length and width and the thermal characteristics of the cell in terms of both absolute heat generation and gradient.

2.2.2. Sensor instrumentation and calibration

To create a *global thermal image* of the cylindrical cell represents a challenging research problem, because of the size and curvature of the cell. Fig. 3(a) shows the pristine cell and the instrumented derivative with the wrapped optical fibre. The length of the optical fibre is 5 m and comprises 63 complete coils or turns from the base of the cell to a value of 4.6 mm below the positive cap. With a spatial resolution of 3 mm along the length of the fibre, this equates to 21 unique measurement locations along each turn of the fibre (circumference) and about 1300 in total along the length of the cell.
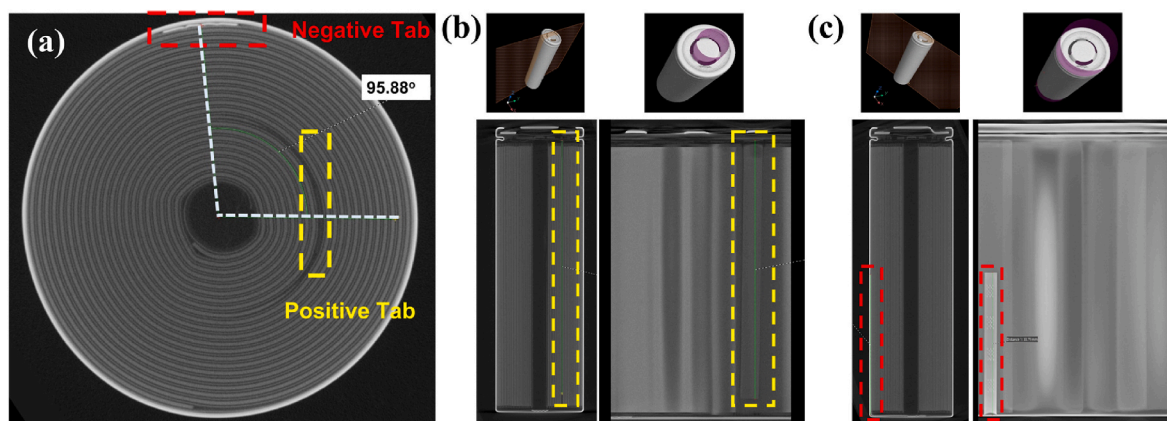
The optical fibre sensor is relatively insensitive to the magnitude of the bend radius as it is wrapped around the cell. To confirm the tight bonding between the cell surface and the optical fibre, a steady force is added on one end of fibre while winding along the cell length. Because the bare optical fibre is sensitive to both temperature and strain, the optical sensor is loosely encapsulated within a 1 mm diameter PTFE tube to insult strain interference.

Due to the thermal resistance of PTFE tube, the temperature calibration of PTFE-encapsulated optical fibre sensor is undertaken, as shown in Fig. 3 (b). Before cell wrapping, a segment of the fibre was placed into a thermal chamber and bonded to a metal plate. A reference thermocouple (RS PRO Type K) was also bonded to the metal plate directly adjacent to the fibre. Due to the 3 mm spatial resolution of the fibre, there are a total of 33-point optical sensors corresponding to the 100 mm segment of fibre. For different temperature set-points, the average value of frequency shifts is calculated for calibration. Fig. 3(b) clearly shows a linear correlation between the measured frequency shift and the temperature variation. The coefficient of correlation is 0.9982 with the optical fibre sensor sensitivity of 1.55 GHz/$^{\circ}$C.

During CT scanning of the candidate cell, the physical locations of both the positive and negative current collectors were defined and marked on the surface of the cell's metal can. To calibrate the start and end locations of the fibre, a heated cube was placed on the first coil (bottom of the cell) in the exact location of the negative tab. The end location of the fibre was determined by placing the same heated cube on the final fibre coil at the top of the cell. Fig. 3(c) clearly shows the temperature increase at these two locations. The fibre's start and end locations are 682.78 mm and 4865.15 mm respectively. Given there are a total of 63 coils of optical fibre along the length of the cell, the average fibre length per coil is estimated at 66.39 mm. This value corresponds well to the theoretical value (πD) of 66.60 mm, given the cell diameter (D) was measured to be 21.2 mm from the CT scan.

The optical measurement accuracy is shown in Fig. 3(d). Optimisation of measurement accuracy and resolution have been discussed in our previous study [26] and will therefore not be repeated here. With a 3 mm resolution, the optical measurement accuracy is limited to within ±0.2 °C.

2.3. Experimental set-up

Fig. 4 presents the experimental setup employed for thermal characterisation of the cell with the optical fibre sensor. After instrumentation, the cell is placed in the holder and connected to the battery test system. A BioLogic VSP 300 is used to control and monitor cell charge and discharge. Additional thermocouple data is recorded via a Pico Logger. The optical fibre sensor is connected to the OFDR interrogator. The instrumented cell is located within the thermal chamber (Binder
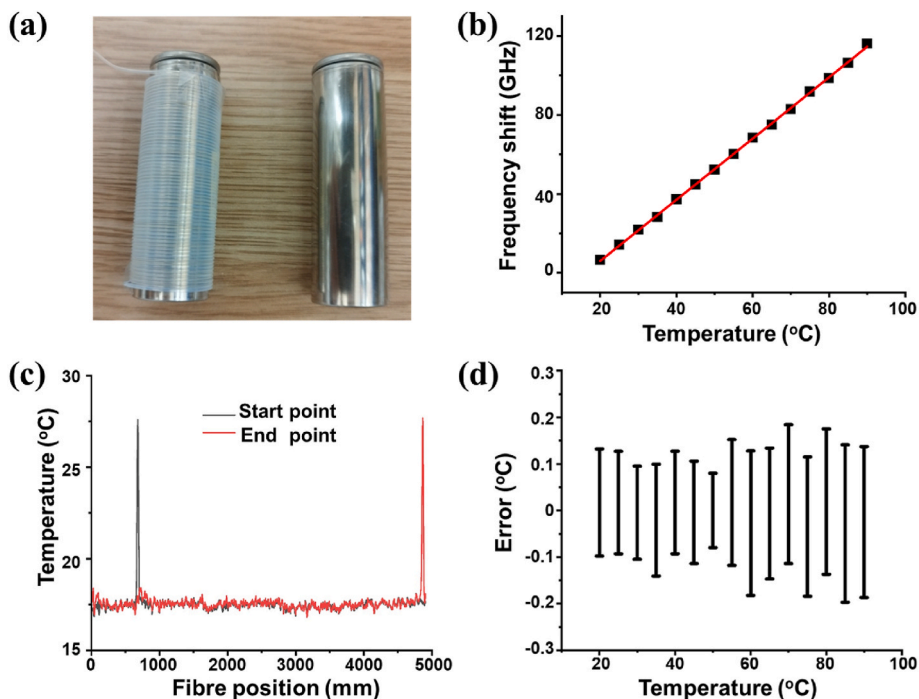

Fig. 2. CT scan of LG INR21700 M50. (a) Cross section in the middle of the cell. (b) Longitudinal section (– left) and unroll view (–right) of positive current tab. (c) Longitudinal section (– left) and unroll view (–right) of negative current tab.

Fig. 3. (a) Instrumented cylindrical cell with winded optical fibre sensor (– left) and pristine cell (–right). (b) Temperature calibration (c) Position calibration of the distributed optical sensor (d) Optical sensor measurement accuracy.
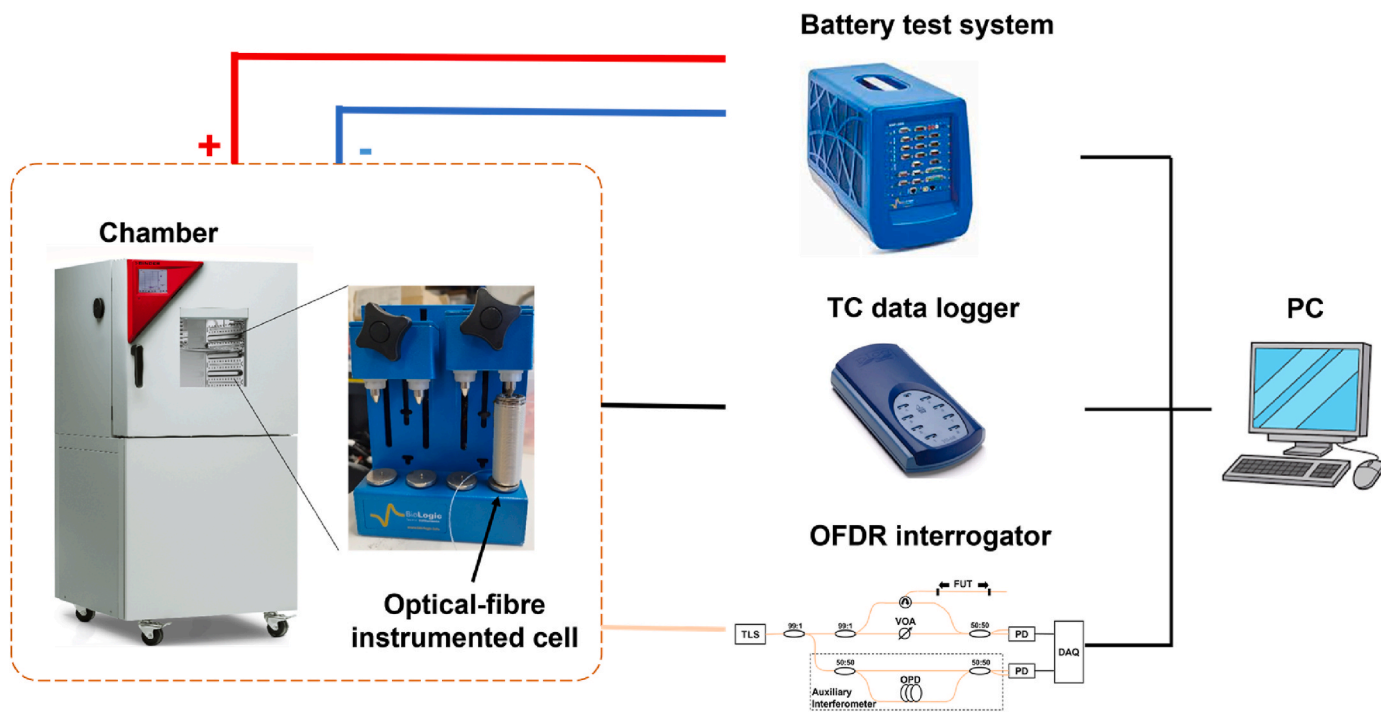

Fig. 4. Experimental setup of global thermal image with distributed optical sensor.

MKF56) to maintain an ambient temperature of 25 °C for the duration of the experiment.

Cell charge and discharge follows a conventional constant current - constant voltage (CC-CV) charge and constant current (CC) discharge protocol. During charge, the cell is charged to the maximum voltage of 4.2V, at which point the voltage is held at the upper limit until the value of current is reduced to C/20. For discharge, a constant current rate is applied to reduce the voltage to the lower limit of 2.5V. Three sets of charge/discharge rates were employed to exercise the cell (1) 0.5C charge - 0.5C discharge; (2) 0.7C charge - 0.7C discharge; and finally (3) 0.7C charge - 1.5C discharge.

3. Experimental results

3.1. Spatial temperature variations

Fig. 5 shows the distributed temperature measurement during the 0.5C discharge - 0.5C charge rate. There are two periods of discharge/charge with a current of 2.425A in Fig. 5(a).

To highlight the value of the OFDR technique, Fig. 5(b) shows two representative points to be discussed in the time domain. Two-dimension coordinate system (h,θ) is defined to locate the points on the surface of cylindrical cells. h represents the point height (unit: mm) from the cell's bottom, while θ is the clockwise angle starting from the centre of the positive current tab. Thus, Point A $(35, 0°)$ is the surface location on the positive tab at middle height of the cell. Conversely, point B $(35, 180°)$ is the same longitudinal location on the cell but on the opposite side to point A. Both measurement locations are within the same fibre coil wrapped around the cell. Their corresponding positions along the optical fibre length is 3175 mm and 3207 mm respectively. Both locations experience the same heat generation profile as the cell in charged and discharge, as a function of cell voltage observed in other publications. It is noteworthy that the peak temperature at point A is circa 1.92 °C higher than that measured at point B (32.03 ± 0.12 °C vs 30.11 ± 0.09 °C) during 0.5C discharge peak, with an average difference of 0.9 °C throughout the profile (average in time-domain). Most publications primarily discuss the temperature gradient that may exist along the axial length of the cell as a function of different cooling strategies [15,16,29,30]. By the proposed distributed sensor and instrumentation, the existence of a thermal gradient along the circumference of the 21700 cell is quantified for the first time.

Fig. 5 (c) shows the spatial temperature distribution at two specific time instances in the experiment (t = 02:39 at 0.5C discharge peak, t = 04:21 at 0.5C charge peak). With the sensing resolution of 3 mm, there are circa 1300 temperature measurement locations within one single fibre. The average temperature of this segment is 30.71 °C under 0.5C discharge, and 29.15 °C under 0.5C charge. The average thermal difference between the time of 0.5C discharge peak and the time of 0.5C

charge peak is 1.56 °C (average in spatial domain).

Regarding the cell surface thermal gradient, measured temperature distribution has a well-defined periodic pattern. The zoom-in of the fibre segment from 3000 mm to 3500 mm are presented in Fig. 5(d). Both patterns have uniform period of about 66.40 mm, which agrees with circumference of the instrumented fibre coil. Moreover, the measured temperature peak and valley are found at the same position under both charge and discharge, indicating a fixed and repeatable profile of the thermal generation regarding to the cell's architecture.

Further 0.7C discharge (CC) - 0.7C charge (CC-CV) and 1.5C discharge (CC) - 0.7C charge (CC-CV) are shown in Fig. 6. The current of 0.7C charge/discharge is 3.395A, while the 1.5C discharge current is 7.275A. With the increasing charge/discharge rate, more heat generation is predicted and observed. For the point-measurement in Fig. 6(a), the temperature on the positive tab (Point A$(35, 0°)$) produces a 33.45 $\pm$ 0.13 °C peak with 0.7C discharge current. Two points (point A$(35, 0°)$ and B$(35, 180°)$) thermal difference at 0.7C discharge peak is measured to be 2.43 °C. With a further increase in discharge rate to 1.5C, the measurement temperature has a significant temperature rise. The discharge temperature peak reaches up to 50.10 $\pm$ 0.15 °C, and the thermal difference between Point A$(35, 0°)$ and B$(35, 180°)$ is 4.31 °C in Fig. 6(b).

It is noted these are just two measurement locations, higher peak-temperature and more obvious thermal gradient can be expected with optical fibre-based distributed measurement. Fig. 6(c) presents the distributed temperature measurement at specific times. The distributed measurement of 0.7C discharge peak and 0.7C charge peak at time of 01:52 and 03:37 (as in Fig. 6(a)) respectively. The distributed measurement of 1.5C discharge peak happens at time of 06:30 (as in Fig. 6 (b)). Take 1.5C discharge for example, the peak temperature of the distributed measurement is 52.85 °C, while the peak temperature of Point A is 50.10 $\pm$ 0.15 °C. The hottest spot is found at $(66, 32.7°)$, near the cell positive cap and aligns to the location of the positive current tab.

As in Fig. 6(c), the measured maximum thermal difference with distributed optical sensor for a 1.5C discharge is 8.37 °C (between the hottest spot 52.85 °C at $(66, 32.7°)$ and coolest spot 44.48 °C at
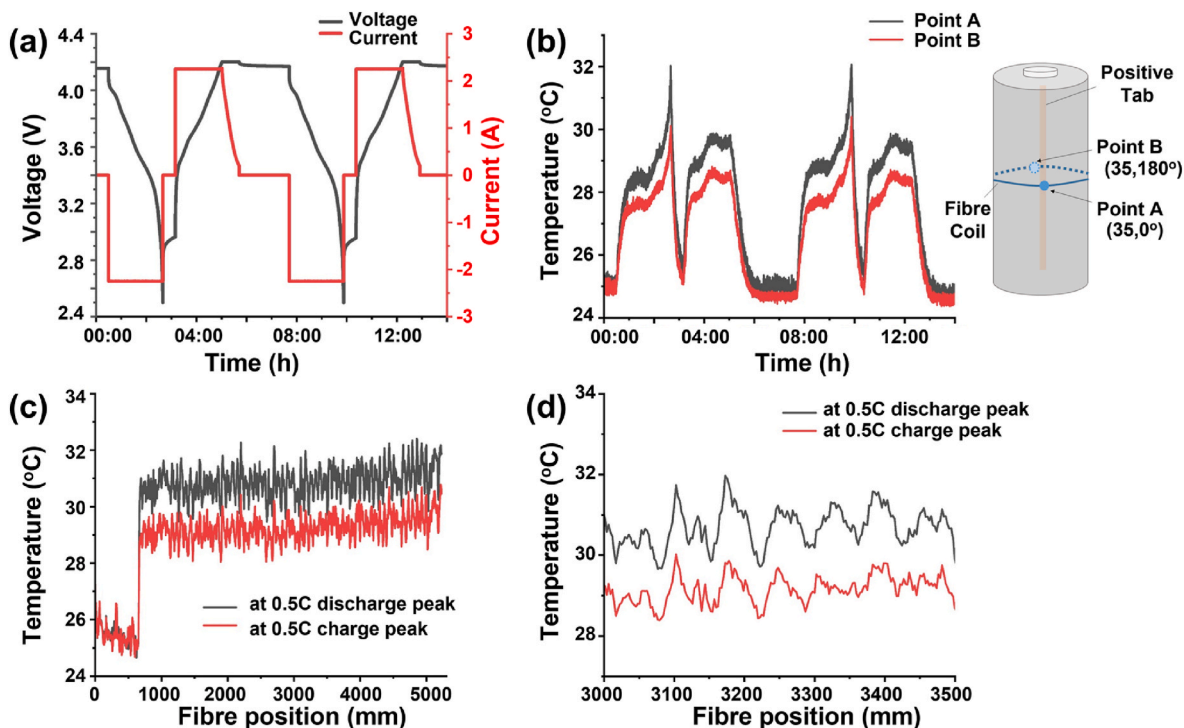

Fig. 5. (a) Current and voltage in the 0.5C discharge – 0.5C charge. (b) Temperature measurement of two specific sensor points. (c) Distributed measurement at the time of charge and discharge temperature peak. (d) Periodic pattern in the distributed measurement.
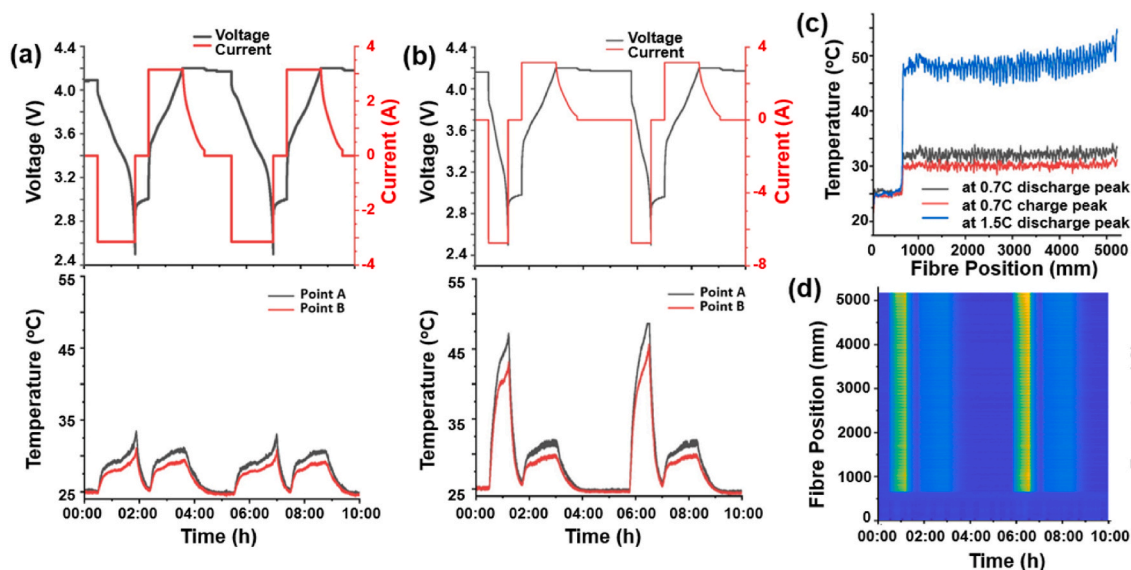
Fig. 6. (a) Current/voltage and temperature measurement in the 0.7C discharge – 0.7C charge. (b) Current/voltage and temperature measurement in the 1.5C discharge – 0.7C charge. (c) Spatial distributed measurement at the time of charge and discharge temperature peak. (d) Distributed temperature measurement under the 1.5C discharge – 0.7C charge.

(30,310.9°)). Conversely, for the two-points, thermal gradient between (A(35, 0°) and B(35, 180°)) is only 4.31 °C, indicating a 194 % difference. With the 1.5C discharge rate, a higher temperature fluctuation is observed with distributed optical sensor, indicating the existence of significant thermal gradient on the cell surface.

Table 1 further shows details about the distributed temperature when the LIB is electrically loaded with different C-rates. It is proved that the proposed distributed optical fibre sensor can deliver accurate determination of the hottest on the cell surface and detailed thermal gradient of cells compared to conventional point-like sensors. These results further highlight that the common practice of placing a thermocouple on the surface of the cell, often simply at the mid-point along its length can lead to unreliable measurements and uncertainty when comparing cell performance evaluated by different organisations, different experiments, or different cells with varying number of internal tabs.

Fig. 6(d) shows the overall distributed measurement in both time and spatial domain under 1.5C discharge - 0.7C charge. Two periods of discharge-charge can be observed in time domain. The periodic pattern in spatial domain is also distinguishable and stable, which will be studied in the following.

3.2. Correlating cell tab location to heat generation

Fig. 7(a) shows how the surface of a 21700 cell can be unrolled to a rectangle with a length of π*21 mm (x axis) and width of 70 mm (y axis). As the global thermal image in Fig. 7(b), the spatial resolution of the optical fibre is 3 mm and 1 mm along the x and y axis respectively. The red zone defined in the figure corresponds to the physical size and location of the positive tab within the cell structure. It becomes clear

how the pattern of heat generation is distributed around the surface of the cell. A correlation can be observed between the higher temperature locations and the interna placement of the positive tab in the cell. The higher temperature fluctuation with 1.5C discharge in Fig. 6(c) can also be explained. The heat is more easily accumulated on the positive tab during the high-rate discharge, which underpins the thermal gradient generation correlating to the tab location.

Of particular interest to this study is the variability around the circumference of the cell (x axis) for the same location along the cell length (y axis). For example, for y = 50 mm, the value of cell temperature varies from 44.94 ± 0.10 °C, 49.41 ± 0.11 °C to 47.71 ± 0.10 °C degrees at locations x = 12 mm, 30 mm, 60 mm respectively. In contrast the placement of the negative tab has much less impact on the magnitude and distribution of cell temperature under electrical load. This result may be counter intuitive, since as shown in Fig. 2, the negative tab is located physically closer to the cell wall. Further research is required to identify why the contribution from the positive and negative tabs vary in this way. Other 21700 cell designs that have multiple tabs will be investigated and validated for a more even temperature distribution. The existence of a temperature gradient along the length of the cell is widely documented [15,16,29,30], in relation to different thermal management strategies. However, to the authors knowledge this is the first time that the magnitude of the temperature gradient has been quantified to this level of spatial resolution with a much greater focus on variations that exist along the circumference of the cell and the corelation of this value to cell tab location.

4. Discussion

The relationship between the thermal gradient and cell's internal architecture has been observed with the proposed distributed optical fibre sensor. To further explore the thermal behaviour and validate the thermal gradient in the 21700 cells, a segment of optical fibre sensor (OFS 1) and a thermocouple (TC 1) are placed directly on the positive cap as shown in in Fig. 8(a). During the cell instrumentation process, both the optical fibre sensor and thermocouples are made sure not to interfere with any battery connections to the experimental rig. OFS 2 and TC 2 are placed in the middle height of the cell, at a location (35, 0°). OFS 3 and TC 3 are placed in the corresponding cell bottom (5, 0°). All thermocouples and corresponding optical fibre are placed as close as possible to confirm the identical point monitor.
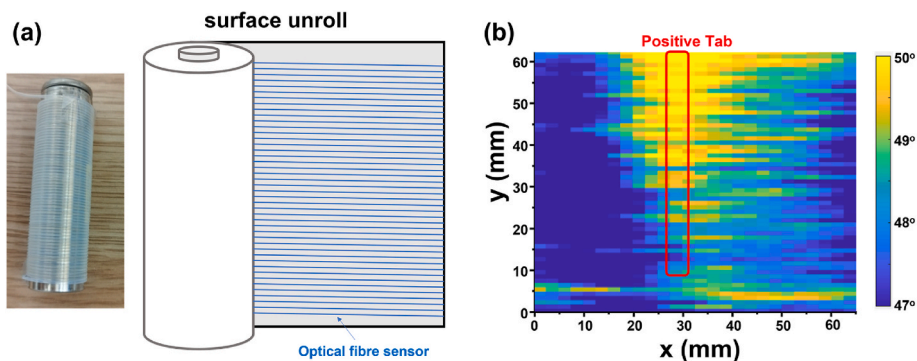
Table 1
Experimental data measured by distributed optical sensor.

C rate	Charge/ Discharge	Max. Temperature	Min. Temperature	Average	ΔT (Max. – Min.)
0.5C	Charge	30.69	28.08	29.29	2.61
	Discharge	32.40	29.46	30.08	2.94
0.7C	Charge	31.43	28.45	30.96	2.98
	Discharge	33.91	30.01	31.94	3.80
1.5C	Discharge	52.85	44.48	49.36	8.37

Fig. 7. (a) Cylinder cell surface unroll and data remapping of distributed optical sensor (b) cell global thermal image at the time of 1.5C discharge temperature peak.
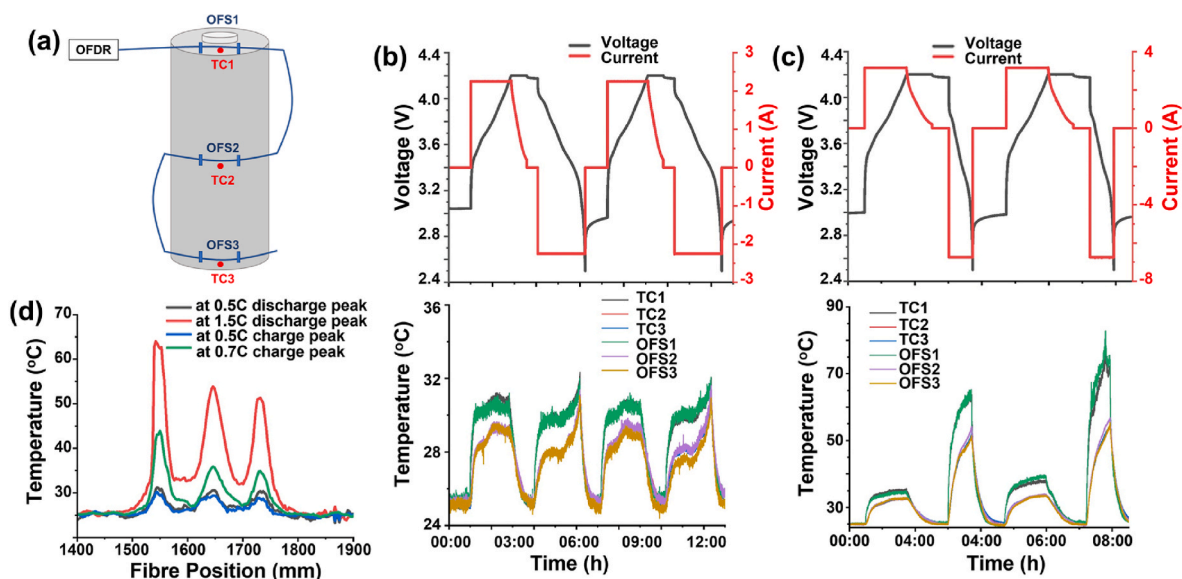

Fig. 8. (a) Schematic of calibration and validation of optical fibre sensor. (b) Current/voltage, optical sensor and thermocouple measurement in the 0.5 charge – 0.5C discharge. (c) Current/voltage, optical sensor and thermocouple measurement in the 0.7 charge – 1.5C discharge (d) Distributed temperature measurement with different charge/discharge rate.

For a 0.5C charge (CC-CV) - 0.5C discharge (CC) and 0.7C charge (CC-CV) and 1.5C discharge (CC) are carried out (Fig. 8(b), (c)). The ambient temperature is controlled to be 25 °C. The measurement agreement between the optical fibre sensor and thermocouples validates the proposed distributed optical measurement. The peak temperature of OFS2-TC2 and OFS3-TC3 are 29.5 °C with a 0.5C charge, while the temperature is 31.08 ± 0.09 °C with a 0.5C discharge. With the increased rates, the peak temperature rises to 33.60 °C with a 0.7C charge and 56.83 °C with a 1.5C discharge, respectively.

The interesting part is instrumented OFS1 and TC1 on the battery positive cap. The measured temperature on the cap is always higher than the ones on the cells surface (OFS2, TC2, OFS3, TC3). The average temperature difference between the cap and the surface is about 1.67 °C with 0.5C charge/discharge. The measured peak temperature on the cap further increases to 82.81 °C with 1.5C discharge as shown in Fig. 8 (c). The corresponding thermal difference increases significantly to 25.98 ± 0.09 °C as well. Together with the surface thermal gradient from positive tab and hottest spot on the positive cap, it will help to guide the relationship between the resistance heat and chemical-mechanical heat during the cell operation in the future investigation.

The spatial distributed measurement at the specific time is further shown in Fig. 8(d). The first peak from 1526 mm to 1578 mm is the fibre segment of OFS1. The OFS2 is from 1614 mm to 1682 mm, while the OFS3 is from 1716 mm to 1762 mm. The corresponding position of TC1,

TC2 and TC3 is located at 1539 mm, 1635 mm and 1723 mm, respectively. In the distributed measurement, the positive cap with OFS1 is always the hottest spot on the cell. Besides, the OFS2, lies in the middle height of the cell, has a higher temperature compared to OFS3, which also agrees with the global thermal image indicated in Fig. 7.

5. Future work

Realisation of distributed optical fibre sensor with fine resolution expands the field boundary of cell design, characterisation and optimisation. Such cylindrical cells global thermal image can be transferred to other format of cells, as pouch cells and prismatic cells, where the thermal gradient is reported to be more sever due to the physical larger size [14,31–33]. Detailed thermal gradient observation provides insight to the thermal management solution. Based on the discovery of particular role of positive current tab in the cylindrical cells, tab architecture/material/numbers/deployment can be priority optimized for a more uniform heat distribution.

Precise temperature distribution measurement for the battery pack is the foundation of battery thermal management system. Sufficient detailed measurement via distributed optical sensor will empower the capability of cell modelling and pack development [34,35]. In future work, the data collected from the distributed sensor can be compared and employed to further parametrise and validate LIB models.

Optical fibre sensor is not only sensitive to temperature, but also able to sense the strain/pressure/ion density et al. [36–38]. The optical fibre sensor has the potential for the multi-physics parameter monitoring, which will give more insight and intrinsic understanding of 'chemical-electrical-thermal-mechanical' insides the cells and packs. The long-distance optical fibre sensor (hundreds of metres) can be further explored for the practical EV battery pack or larger containerised power storage for grid applications.

This developed OFDR utilise a tuneable laser source and commercial telecom fibre as a sensor, which means the sensor unit costs little (less than 1£/m). Most budget of the optical interrogator is the tuneable laser source, whose price is currently high for the practical BMS/BTMS. During thermal sensor instrumentation, the optical measurement can help to identify and locate the place of interest for the low-cost thermocouples. Eventually, future study of the price friendly silicon-based laser source [39,40] and external wavelength modulation [41,42] should be focused for the budget control.

6. Conclusion

OFDR-based distributed optical fibre sensor is proposed to deliver a global thermal image of a cylindrical 21700 cell. The cell is instrumented by winding the optical fibre around the cell surface. Distributed measurement with a 3 mm spatial resolution, for the first time, helps to reveal a detailed thermal gradient of the cell. The temperature variation along the circumference of the cell is firstly discovered. Proposed global thermal image further helps to identify the heat accumulation around the positive current tab under the cell high-rate discharge. The result indicates the common existence of thermal gradient even within one compact 21700 cell. Large format cells (pouch and prismatic) and modules/packs are expected to experience more severe thermal gradients. The global thermal image also helps to investigate the cell heat behaviour, as heat generation, transmission and dissipation under different conditions. Therefore, such distributed optical sensor is believed to be an effective and high-performance method for the further design and optimisation of battery and energy applications.

CRediT authorship contribution statement

Zhen Guo: Conceptualization, Data curation, Formal analysis, Investigation, Methodology, Visualization, Writing – original draft, Writing – review & editing. **Calum Briggs:** Data curation, Investigation, Methodology. **Timothy A. Vincent:** Investigation, Writing – review & editing. **Begum Gulsoy:** Formal analysis, Investigation, Methodology. **Jonathan E.H. Sansom:** Formal analysis, Investigation. **James Marco:** Conceptualization, Project administration, Writing – review & editing.

Declaration of competing interest

The authors declare that they have no known competing financial interests or personal relationships that could have appeared to influence the work reported in this paper.

Data availability

Data will be made available on request.

Acknowledgement

References

[1] Peiyi Sun, Roeland Bisschop, Huichang Niu, Xinyan Huang, A review of battery fires in electric vehicles, Fire Technol. 56 (2020) 1361–1410.

[2] Nicholas Williard, Wei He, Christopher Hendricks, Michael Pecht, Lessons learned from the 787 dreamliner issue on lithium-ion battery reliability, Energies 6 (9) (2013) 4682–4695.

[3] Melanie J. Loveridge, Guillaume Remy, Nadia Kourra, Ronny Genieser, Anup Barai, Mike J. Lain, Yue Guo, et al., Looking deeper into the galaxy (Note 7), Batteries 4 (1) (2018) 3.

[4] Kai Liu, Yayuan Liu, Dingchang Lin, Allen Pei, Yi Cui, Materials for lithium-ion battery safety, Sci. Adv. 4 (6) (2018), eaas9820.

[5] Jang-Hoon Park, Joo-Hyun Cho, Woong Park, Dongjo Ryoo, Su-Jin Yoon, Jong Hun Kim, Yeon Uk Jeong, Sang-Young Lee, Close-packed SiO2/poly (methyl methacrylate) binary nanoparticles-coated polyethylene separators for lithium-ion batteries, J. Power Sources 195 (24) (2010) 8306–8310.

[6] Kai Liu, Allen Pei, Hye Ryoung Lee, Biao Kong, Nian Liu, Dingchang Lin, Yayuan Liu, et al., Lithium metal anodes with an adaptive "solid-liquid" interfacial protective layer, J. Am. Chem. Soc. 139 (13) (2017) 4815–4820.

[7] Katsuhiko Naoi, Etsuro Iwama, Nobuhiro Ogihara, Yasuhiro Nakamura, Haruki Segawa, Yuji Ino, Nonflammable hydrofluoroether for lithium-ion batteries: enhanced rate capability, cyclability, and low-temperature performance, J. Electrochem. Soc. 156 (4) (2009) A272.

[8] Ryoji Kanno, Masahiro Murayama, Lithium ionic conductor thio-LISICON: the Li2 S GeS2 P 2 S 5 system, J. Electrochem. Soc. 148 (7) (2001) A742.

[9] Xing-Yan Yao, Michael G. Pecht, Tab design and failures in cylindrical Li-ion batteries, IEEE Access 7 (2019) 24082–24095.

[10] Minggao Ouyang, Xuning Feng, Xuebing Han, Languang Lu, Zhe Li, Xiangming He, A dynamic capacity degradation model and its applications considering varying load for a large format Li-ion battery, Applied energy 165 (2016) 48–59.

[11] Ahmad A. Pesaran, Battery thermal models for hybrid vehicle simulations, J. Power Sources 110 (2) (2002) 377–382.

[12] J. Warner, Chapter 7: lithium-ion battery packs for EVs, in: Lithium-Ion Batteries: Advances and Applications, Elsevier, Amsterdam, The Netherlands, 2014, pp. 127–150.

[13] G. Zhang, L. Cao, S. Ge, C.Y. Wang, C.E. Shaffer, C.D. Rahn, In situ measurement of radial temperature distributions in cylindrical Li-ion cells, J. Electrochem. Soc. 161 (10) (2014) A1499.

[14] I.A. Hunt, Y. Zhao, Y. Patel, G. Offer, Surface cooling causes accelerated degradation compared to tab cooling for lithium-ion pouch cells, J. Electrochem. Soc. 163 (9) (Jul. 2016). A1846eA1852.

[15] Yifei Yu, Timothy Vincent, Jonathan Sansom, David Greenwood, James Marco, Distributed internal thermal monitoring of lithium ion batteries with fibre sensors, J. Energy Storage 50 (2022), 104291.

[16] Timothy A. Vincent, Begum Gulsoy, Jonathan EH. Sansom, James Marco, In-situ instrumentation of cells and power line communication data acquisition towards smart cell development, J. Energy Storage 50 (2022), 104218.

[17] M. Akbarzadeh, T. Kalogiannis, J. Jaguemont, J. He, L. Jin, M. Berecibar, J. Van Mierlo, Thermal modeling of a high-energy prismatic lithium-ion battery cell and module based on a new thermal characterization methodology, J. Energy Storage 32 (2020), 101707.

[18] Orhan Kalkan, Celen Ali, Kadir Bakirci, Experimental and numerical investigation of the LiFePO4 battery cooling by natural convection, J. Energy Storage 40 (2021), 102796.

[19] Gaoce Han, Jize Yan, Zhen Guo, David Greenwood, James Marco, Yifei Yu, A review on various optical fibre sensing methods for batteries, Renew. Sustain. Energy Rev. 150 (2021), 111514.

[20] Gang Yang, Catia Leitão, Yuhong Li, João Pinto, Xuefan Jiang, Real-time temperature measurement with fiber Bragg sensors in lithium batteries for safety usage, Measurement 46 (9) (2013) 3166–3172.

[21] Susana Novais, Micael Nascimento, Lorenzo Grande, Maria Fátima Domingues, Paulo Antunes, Nélia Alberto, Cátia Leitão, et al., Internal and external temperature monitoring of a Li-ion battery with fiber Bragg grating sensors, Sensors 16 (9) (2016) 1394.

[22] Lucca C. Matuck, Pedro D. Cabrita, João L. Pinto, Carlos A. Marques, Micael S. Nascimento, Customized optical fiber birefringent sensors to multipoint and simultaneous temperature and radial strain tracking of lithium-ion batteries, Advanced Sensor Research (2023), 2200046.

[23] Rao Yunjiang, Zinan Wang, Huijuan Wu, Zengling Ran, Bing Han, Recent advances in phase-sensitive optical time domain reflectometry (Φ-OTDR), Photonic Sensors 11 (1) (2021) 1–30.

[24] Xiaoyi Bao, Zichao Zhou, Yuan Wang, Distributed time-domain sensors based on Brillouin scattering and FWM enhanced SBS for temperature, strain and acoustic wave detection, PhotoniX 2 (2021) 1–29.

[25] Brian J. Soller, K. Gifford Dawn, Matthew S. Wolfe, Mark E. Froggatt, High resolution optical frequency domain reflectometry for characterization of components and assemblies, Opt Express 13 (2) (2005) 666–674.

[26] Zhen Guo, Jize Yan, Gaoce Han, David Greenwood, James Marco, Yifei Yu, High sensing accuracy realisation with millimetre/sub-millimetre resolution in optical frequency domain reflectometer, J. Lightwave Technol. 40 (12) (2022) 4050–4056.

[27] Zhen Guo, Gaoce Han, Jize Yan, David Greenwood, James Marco, Yifei Yu, Ultimate spatial resolution realisation in optical frequency domain reflectometry with equal frequency resampling, Sensors 21 (14) (2021) 4632.

[28] Mark Froggatt, Jason Moore, High-spatial-resolution distributed strain measurement in optical fiber with Rayleigh scatter, Appl. Opt. 37 (10) (1998) 1735–1740.

[29] Renjing Gao, Zhaohui Fan, Shutian Liu, A gradient channel-based novel design of liquid-cooled battery thermal management system for thermal uniformity improvement, J. Energy Storage 48 (2022), 104014.

[30] Christoph Bolsinger, Kai Peter Birke, Effect of different cooling configurations on thermal gradients inside cylindrical battery cells, J. Energy Storage 21 (2019) 222–230.

[31] Dongdong Li, Lin Yang, Identification of spatial temperature gradient in large format lithium battery using a multilayer thermal model, Int. J. Energy Res. 44 (1) (2020) 282–297.

[32] Thomas George Tranter, Robert Timms, Paul R. Shearing, D.J.L. Brett, Communication—prediction of thermal issues for larger format 4680 cylindrical cells and their mitigation with enhanced current collection, J. Electrochem. Soc. 167 (16) (2020), 160544.

[33] Markus Gepp, Filimon Radu, Stéphane Koffel, Vincent RH. Lorentz, März Martin, Advanced thermal management for temperature homogenization in high-power lithium-ion battery systems based on prismatic cells, in: 2015 IEEE 24th International Symposium on Industrial Electronics (ISIE), IEEE, 2015, pp. 1230–1235.

[34] Jiayuan Lin, Xinhua Liu, Li Shen, Cheng Zhang, Shichun Yang, A review on recent progress, challenges and perspective of battery thermal management system, Int. J. Heat Mass Tran. 167 (2021), 120834.

[35] Z.Y. Jiang, H.B. Li, Z.G. Qu, J.F. Zhang, Recent progress in lithium-ion battery thermal management for a wide range of temperature and abuse conditions, Int. J. Hydrogen Energy 47 (15) (2022) 9428–9459.

[36] Jun Peng, Shuhai Jia, Shuming Yang, Xilong Kang, Hongqiang Yu, Yaowen Yang, State estimation of lithium-ion batteries based on strain parameter monitored by fiber Bragg grating sensors, J. Energy Storage 52 (2022), 104950.

[37] Albero Blanquer, Laura, Florencia Marchini, Jan Roman Seitz, Nour Daher, Fanny Bétermier, Jiaqiang Huang, Charlotte Gervillié, Jean-Marie Tarascon, Optical sensors for operando stress monitoring in lithium-based batteries containing solid-state or liquid electrolytes, Nat. Commun. 13 (1) (2022) 1153.

[38] Runlin Wang, Haozhe Zhang, Qiyu Liu, Liu Fu, Xile Han, Xiaoqing Liu, Kaiwei Li, et al., Operando monitoring of ion activities in aqueous batteries with plasmonic fiber-optic sensors, Nat. Commun. 13 (1) (2022) 547.

[39] Minh A. Tran, Duanni Huang, John E. Bowers, Tutorial on narrow linewidth tunable semiconductor lasers using Si/III-V heterogeneous integration, APL photonics 4 (2019) 11.

[40] Hang Guan, Ari Novack, Tal Galfsky, Yangjin Ma, Saeed Fathololoumi, Alexandre Horth, Tam N. Huynh, et al., Widely-tunable, narrow-linewidth III-V/silicon hybrid external-cavity laser for coherent communication, Opt Express 26 (7) (2018) 7920–7933.

[41] Dian Chen, Qingwen Liu, Zuyuan He, Phase-detection distributed fiber-optic vibration sensor without fading-noise based on time-gated digital OFDR, Opt Express 25 (7) (2017) 8315–8325.

[42] Zhaopeng Zhang, Xinyu Fan, Zuyuan He, Long-range and wide-band vibration sensing by using phase-sensitive OFDR to interrogate a weak reflector array, Opt Express 28 (12) (2020) 18387–18396.